



Article

Landslide Mapping in Calitri (Southern Italy) Using New Multi-Temporal InSAR Algorithms Based on Permanent and Distributed Scatterers

Nicola Angelo Famiglietti ¹, Pietro Miele ^{1,*}, Marco Defilippi ², Alessio Cantone ², Paolo Riccardi ², Giulia Tessari ² and Annamaria Vicari ¹

¹ Istituto Nazionale di Geofisica e Vulcanologia, Sezione Irpinia, 83035 Grottaminarda, Italy; nicola.famiglietti@ingv.it (N.A.F.); annamaria.vicari@ingv.it (A.V.)

² SarmapSA, 6987 Caslano, Switzerland; mdefilippi@sarmap.ch (M.D.); acantone@sarmap.ch (A.C.); priccardi@sarmap.ch (P.R.); gtessari@sarmap.ch (G.T.)

* Correspondence: pietro.miele@ingv.it; Tel.: +39-0825446481

Abstract: Landslides play a significant role in the morpho-evolutional processes of slopes, affecting them globally under various geological conditions. Often unnoticed due to low velocities, they cause diffuse damage and loss of economic resources to the infrastructure or villages built on them. Recognizing and mapping mass movements is crucial for mitigating economic and social impacts. Conventional monitoring techniques prove challenging for large areas, necessitating resource-intensive ground-based networks. Leveraging abundant synthetic aperture radar (SAR) sensors, satellite techniques offer cost-effective solutions. Among the various methods based on SAR products for detecting landslides, multi-temporal differential interferometry SAR techniques (MTInSAR) stand out for their precise measurement capabilities and spatiotemporal evolution analysis. They have been widely used in several works in the last decades. Using information from the official Italian landslide database (IFFI), this study employs Sentinel-1 imagery and two new processing chains, E-PS and E-SBAS algorithms, to detect deformation areas on the slopes of Calitri, a small town in Southern Italy; these algorithms assess the cumulated displacements and their state of activity. Taking into account the non-linear trends of the scatterers, these innovative algorithms have helped to identify a dozen clusters of points that correspond well with IFFI polygons.

Keywords: MTInSAR; landslide; remote sensing; permanent and distributed scatterers; E-PS; E-SBAS



Citation: Famiglietti, N.A.; Miele, P.; Defilippi, M.; Cantone, A.; Riccardi, P.; Tessari, G.; Vicari, A. Landslide Mapping in Calitri (Southern Italy) Using New Multi-Temporal InSAR Algorithms Based on Permanent and Distributed Scatterers. *Remote Sens.* **2024**, *16*, 1610. <https://doi.org/10.3390/rs16091610>

Academic Editor: Fumio Yamazaki

Received: 20 March 2024

Revised: 23 April 2024

Accepted: 28 April 2024

Published: 30 April 2024



Copyright: © 2024 by the authors. Licensee MDPI, Basel, Switzerland. This article is an open access article distributed under the terms and conditions of the Creative Commons Attribution (CC BY) license (<https://creativecommons.org/licenses/by/4.0/>).

1. Introduction

Landslides, deep or shallow, are important agents in morpho-evolution processes. These mass movements, affecting slope stability in many regions of the world, are related to a variety of geological conditions and other predisposing factors due to their initiation and evolution [1–3].

Mass movements can vary, based on the involved material, their kinematics, and velocity [4–6]. In some cases, these phenomena have proven to be catastrophic events causing numerous victims and considerable damage; in other cases, due to their extremely low velocity (mm or cm per year), landslides can remain unknown or very difficult to recognize for a long time. So, roads, buildings, and infrastructure are often built on them. This condition is widespread in many regions throughout the world and a large number of towns suffer diffuse damage induced by active landslides or by periodical reactivation [7–12]. Identifying and mapping landslides is essential for mitigating their economic and social impact. Landslide Inventory Maps (LIMs), periodically updated with information on the state of activity, are the main tools supporting the expansion planning of urbanized areas [13].

Among the various cases already known in the literature, the landslides involving the town of Calitri, located in the Avellino province, Italy, represent some of the most famous and studied reactivated mass movements triggered by earthquakes [14,15].

To investigate large areas affected by numerous slope failures for long periods, including Calitri, the use of conventional monitoring techniques (e.g., total stations, global navigation satellite system (GNSS) receivers, extensometers, tilt-meters, inclinometers, etc.) proves to be difficult and resource-intensive. Ground-based monitoring networks are often economically unsustainable, and technical limitations, such as inaccessibility to landslide sites, and management costs of the installed instrumentation, hamper the availability of extensive studies of unstable slopes.

Considering the abundance of synthetic aperture radar (SAR) sensors, products, and data processing algorithms, satellite techniques allow for the detection of areas affected by ground deformation induced by both natural hazards and human activities at different scales [16–20]. The detection and mapping of landslides, using SAR images, can be performed through polarimetric techniques [21,22], coherence [23,24], or amplitude change detection of pre- and post-failure images [25–28].

However, although all the above-mentioned techniques are capable of detecting areas affected by landslides, in many cases, they are not able to provide accurate measurements of the ground surface displacements or reconstruct the spatiotemporal evolution. To conduct this, the use of multi-temporal interferometry SAR techniques (MTInSAR) [29–32] can be advantageous for mapping landslide phenomena as well as for determining their state of activity in the long run [33,34]. Data acquired by space-borne SAR sensors and processed using differential SAR interferometry (DInSAR) techniques are now important technological tools in landslide investigations and studies [35–39].

Several MTInSAR applications for landslide mapping can be found worldwide and in Italy, adopting different approaches [40–42], data, and workflows implemented. Moreover, these techniques have demonstrated their capability to reach measurement precision of about 1–2 mm/year for deformation velocity maps and time series [43–45].

This study is focused on detecting landslides that impact both the northern and southern slopes of Calitri hill, where the main slope failure occurred. Their presence and state of activity have been assessed through field evidence and the employment of new MTInSAR algorithm analysis, specifically Enhanced-PS (E-PS) and Enhanced-SBAS (E-SBAS). The collected Sentinel-1 imagery has been used to verify and possibly update the state of activity of the known and mapped landslides in the Italian Landslide Inventory, IFFI, produced by the Italian Institute for Environmental Protection and Research [46].

2. Study Area

Calitri is located 25 km from the Mount Vulture volcanic complex and about 150 km east of Naples.

Specifically, the town of Calitri lies on the left bank of the Ofanto River, set on a hilly morphology characterized by marine sedimentary Pliocene regressive successions, including clays and silty gray–blue clays, sandstones, sands, and conglomerates. In the middle-lower portion of the hilly relief, as well as in some areas of the town, clays outcrop (Red Flysch or varicolored clays, Figure 1).

Apennine tectonics, which began in the Middle–Upper Miocene and continued throughout the Plio–Pleistocene, comported large-scale dislocations and associated intensive deformations in the rock units [47].

Since historical times, the slopes of Calitri hill [48] have been affected by a large number of landslides, mainly complex (roto-translational evolved into earthflow), involving the pelitic terms (silty and marly clays, sands) of the Ariano Irpino Super-Synthem. The town of Calitri is well known worldwide for its large landslide reactivated by the 23 November 1980 seismic event affecting the southern slope [49–51]. In addition, other active landslides are present on the northern slopes of the built-up area that are part of the Cortino basin. According to the IFFI database (Inventario dei Fenomeni Franosi in Italia,

<https://idrogeo.isprambiente.it/app/iffi/>, accessed on 10 January 2024), updated to 2006, slopes are affected by many mass movements, which consist of roto-translational and earth flow dormant landslides.

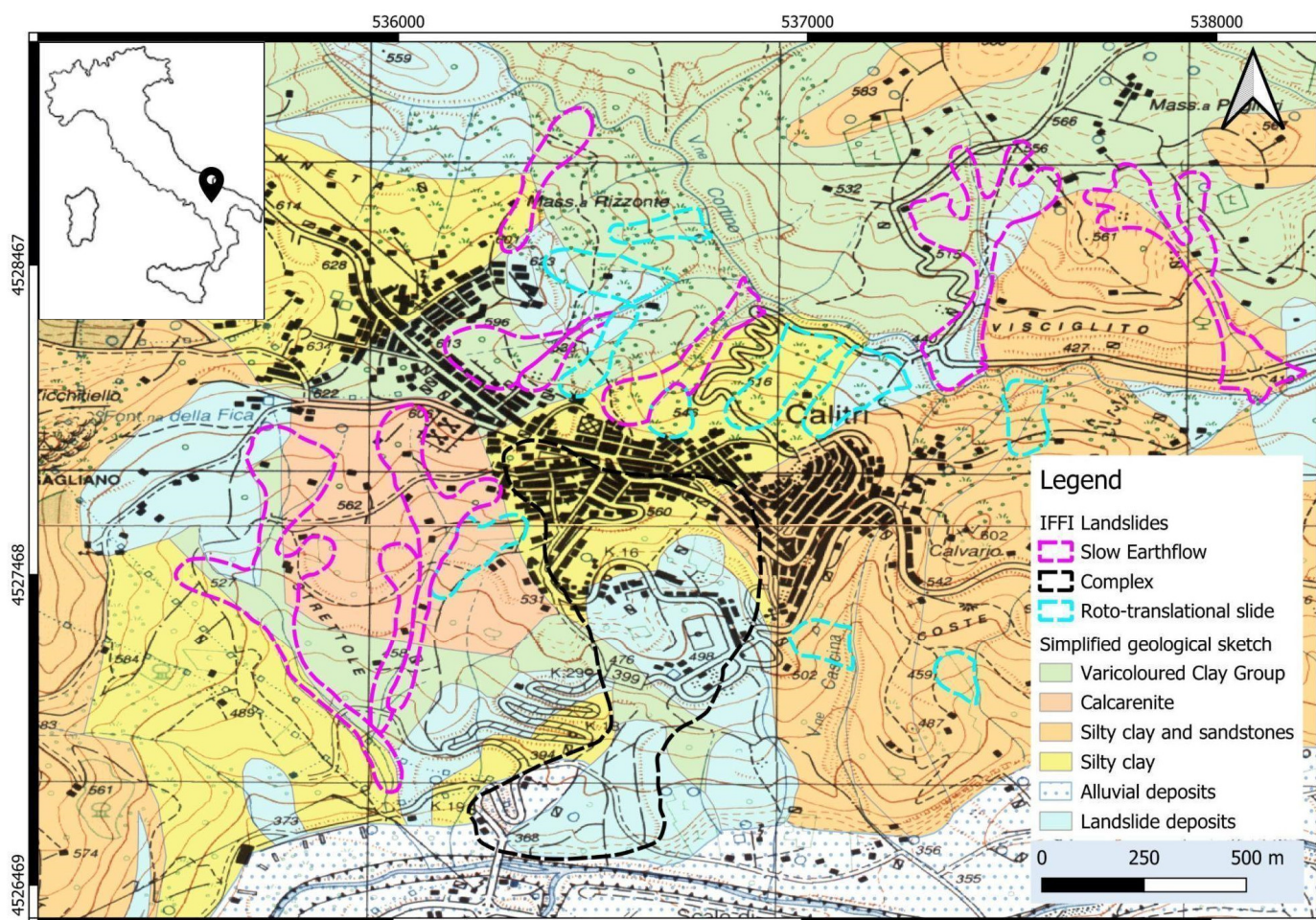


Figure 1. Geological setting of the study area. The represented lithologies have been extracted from sheet n. 451 “Melfi” released by ISPRA within the CARG project (https://www.isprambiente.gov.it/Media/carg/451_MELFI/Foglio.html, accessed on 10 January 2024).

3. Materials and Methods

In the MTInSAR analysis, C-band SAR images from the Sentinel-1 satellite (provided by ESA) were utilized. These images were acquired along both ascending and descending orbit tracks. Specifically, products with the Interferometric-Wide (IW) acquisition mode and VV polarization were employed. Two stacks of scenes were examined, covering the period from January 2015 to December 2023 considering 1 acquisition per month, with 108 scenes along both orbits, as seen in Table 1.

Table 1. The Sentinel-1 satellite’s relative paths, frames, incidence angles, and the number of scenes across both orbits.

Satellite	Orbit	Path	Frame	Incidence Angle	Nr. Scenes
Sentinel-1	Ascending	44	127	42.29	108
	Descending	124	457	38.76	108

Deformation analysis can be categorized into two main categories based on surface backscatter: persistent scatterer (PS) and distributed scatterer (DS). On the one hand, PSs

are objects characterized by a high signal-to-noise ratio and often appear as consistently bright and stable points over time, commonly associated with man-made features [52]. On the other hand, DSs exhibit an average or low signal-to-noise ratio and can be utilized effectively when they form homogeneous groups of pixels that are large enough to allow statistical analysis. These clusters can maintain their coherence over time, even intermittently, as typically observed in rural areas [53]. Historical approaches that can independently measure either DS or PS are the small baseline subset (SBAS) and persistent scatterer interferometry (PSI), respectively. Over the past decade, significant advancements in this field have introduced new methods that are capable of concurrently extracting measurements from both PS and DS.

These advancements have been integrated into SARscape® V. 5.7.0 software, which introduces two innovative processing chains: Enhanced SBAS (E-SBAS) and Enhanced PS (E-PS). These new methodologies build on the foundations of the original PS and SBAS techniques, as established by Ferretti et al. [54] and Berardino et al. [55]. By integrating these enhanced processing chains, researchers can now more effectively harness the capabilities of both PS and DS analyses, leading to more precise deformation studies. The data quality control process includes the removal of the phase noise, where the flattened interferograms are multi-looked and filtered, typically using a Goldstein filter. In the case of E-PS, the filtering is applied only to the DS, by using adaptive spatial phase multi-look.

Each technique offers different characteristics in terms of absolute precision, the ability to manage non-continuous or non-linear historical time series, and coverage. The ALOS World 3D (AW3D30) Digital Elevation Model (DEM), with a resolution of 30 m, was utilized to remove topography from generated interferograms to achieve accurate ground deformations. To remove atmospheric phase components, the atmospheric phase screen (APS) filter is used [56]. Moreover, to obtain reliable deformation measurements and to optimize the displacement trend assessment as a Ground Control Point (GCP) during the geocoding processing step, the AVO4 geodetic network's station of INGV was selected (<http://ring.gm.ingv.it/>, accessed on 10 January 2024).

3.1. Enhanced PS (E-PS)

The E-PS approach is inspired by Ferretti et al. [57] and Fornaro et al. [58]. The joint processing of PS and DS can be carried out independently, without the need for significant changes in the standard PS processing chain (Figure 2). Such an approach is aimed at extending the standard PS analysis on rural areas, and in this regard, two main steps are needed:

1. The identification of pixel examples that are similar from a statistical point of view must be performed. The Kolmogorov–Smirnov (KS) and Anderson–Darling (AD) tests are both based on the amplitude of the co-registered and calibrated stack of SAR data. These tests are specifically designed to detect distributed scatterers (DSs);
2. For all of the DSs identified by statistical tests, the covariance matrix that takes advantage of the ensemble of similar pixels is estimated. SLC phases in correspondence with DS are weighted optimally, either by the maximum likelihood estimator (MLE) under the assumption of Gaussianity, or by exploiting the largest principal component of the covariance matrix. The final estimate of the time series of displacement should be made by processing the DS that has a consistency above a certain threshold with the PS.

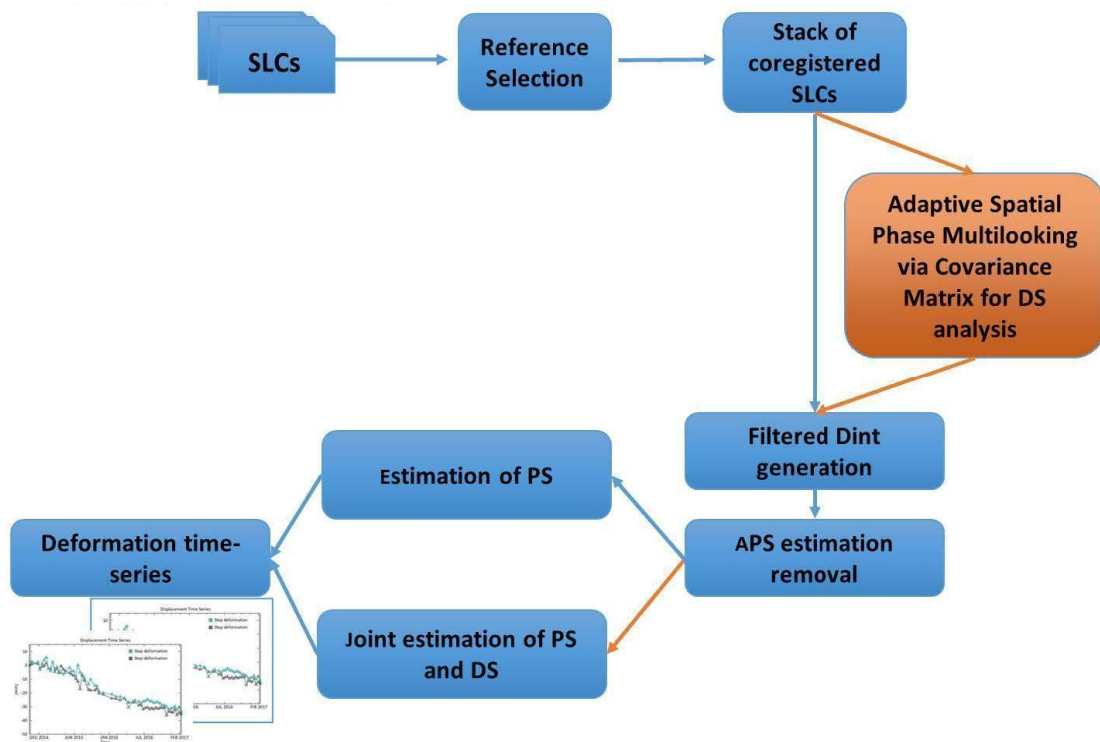


Figure 2. E-PS workflow.

3.2. Enhanced SBAS (E-SBAS)

The E-SBAS consists of the integration of the standard SBAS processing chain, according to Berardino et al. [55], where outputs initialize a PS approach [59] to retrieve precise deformation information about strong and stable reflectors (therefore, the PS targets).

The functionality of the E-SBAS technique is two-fold as shown in Figure 3:

- I. Estimates the low-pass deformation time series, specifically at the locations of distributed scatterer (DS) points;
- II. Estimates the low-pass digital elevation model (DEM)—residual topography.

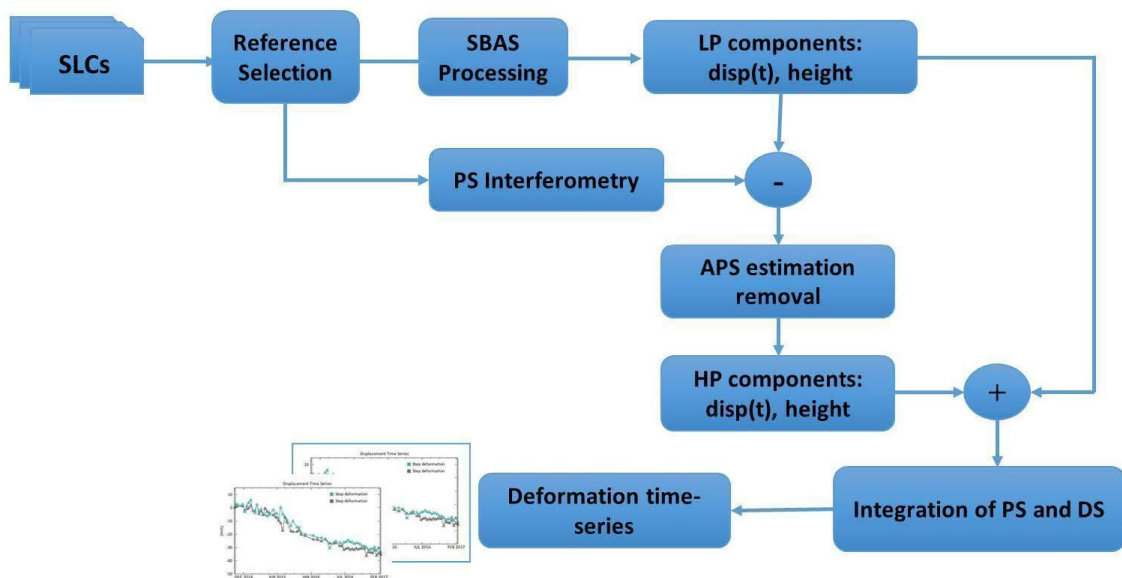


Figure 3. E-SBAS workflow.

The temporal displacement associated with PS points is obtained by applying the PSI method to interferograms that were previously calibrated, removing the low-pass topography, deformation, and residual atmosphere estimated by the SBAS technique. This strategy integrates the PSI and SBAS methods, ensuring the consistency of deformation results obtained at point-like and DS targets and, therefore, provides better results concerning the approach of executing the two methods independently from each other. The proposed hybrid approach is not just the simple application of the two techniques independently; indeed, the method is able to analyze both strong reflectors and distributed targets, delivering lower-resolution DS results combined with higher-resolution PS for even non-linear trends in an integrated continuous spatial solution.

In this case study, the minimum temporal baseline considered is 12 and the maximum is equal to 180 (days) with minimum normal baseline redundancy criteria.

4. Results

The analysis yielded a significant number of points suitable for monitoring in the areas surrounding the town. Table 2 summarizes the outcomes for each algorithm chain used, including the total number of points and their density across Calitri, covering an extension of approximately 2 square kilometers.

Table 2. Results overview of the applied algorithms on the territory surrounding the study area.

Algorithms.	Points Number (1.85 km ²)	Points Density (km ²)	Points Density (ha)
PS	9795	5295	53
E-PS	14,581	7881	79
SBAS	7537	4074	40
E-SBAS	11,800	6378	64

As expected, for urban area applications, a substantial number of points was obtained using the PS and SBAS algorithms. Additionally, the hybrid approach underlying the E-PS and E-SBAS chains increased the point count by over 60%. The subsequent sub-sections present a detailed overview of the outcomes generated by these two new algorithms, followed by a discussion on the points' distribution and time series patterns observed.

4.1. E-PS Velocity Maps

The ground deformation detected along the line of sight (LoS) by E-PS from both ascending and descending datasets allowed us to obtain the vertical and E-W deformation maps within the SARscape[®] environment [60,61], as presented in Figure 4A,B. The velocity of all points, namely enhanced permanent scatterers (E-PSs) within the study area, was evaluated by identifying the stability range between 2 and -2 mm/year. According to these criteria, for the vertical deformation map, we identified 703 non-stable points, which represent about 5% of the 14,581 total points. All unstable points detected are characterized by negative velocity, except a cluster (uplift) of 10 located in the northwest area of the football stadium (Figure 4A).

These E-PSs are concentrated in two clearly identifiable clusters on the map and located both on the south and the north slopes of the village of Calitri. As predictable, points are located in the built-up areas and none of them are in the vegetated areas. The main cluster on the south slope is composed of 150 E-PSs with velocities ranging from -5 to -2 mm/yr, and it is within the landslide area detected in several previous works. The other cluster is located on slopes of the Cortino stream basin and includes 120 E-PSs characterized by a velocity larger than -2 mm/yr.

Considering Figure 4B, representing the E-W velocity map, the detectable features are quite different. Also, in this case, a cluster in the upper part of the southern slope of the village composed of 242 E-PSs with negative velocity, westward, is evident. In addition, an additional cluster that is quite extended on the west side of the hill, characterized by

positive velocity, eastbound (184 blue dots on the map), is evident. No unstable point is detectable on the north side; instead, there are other points with negative velocity distributed throughout the middle of the southern slope, very close to the football stadium and the national road.

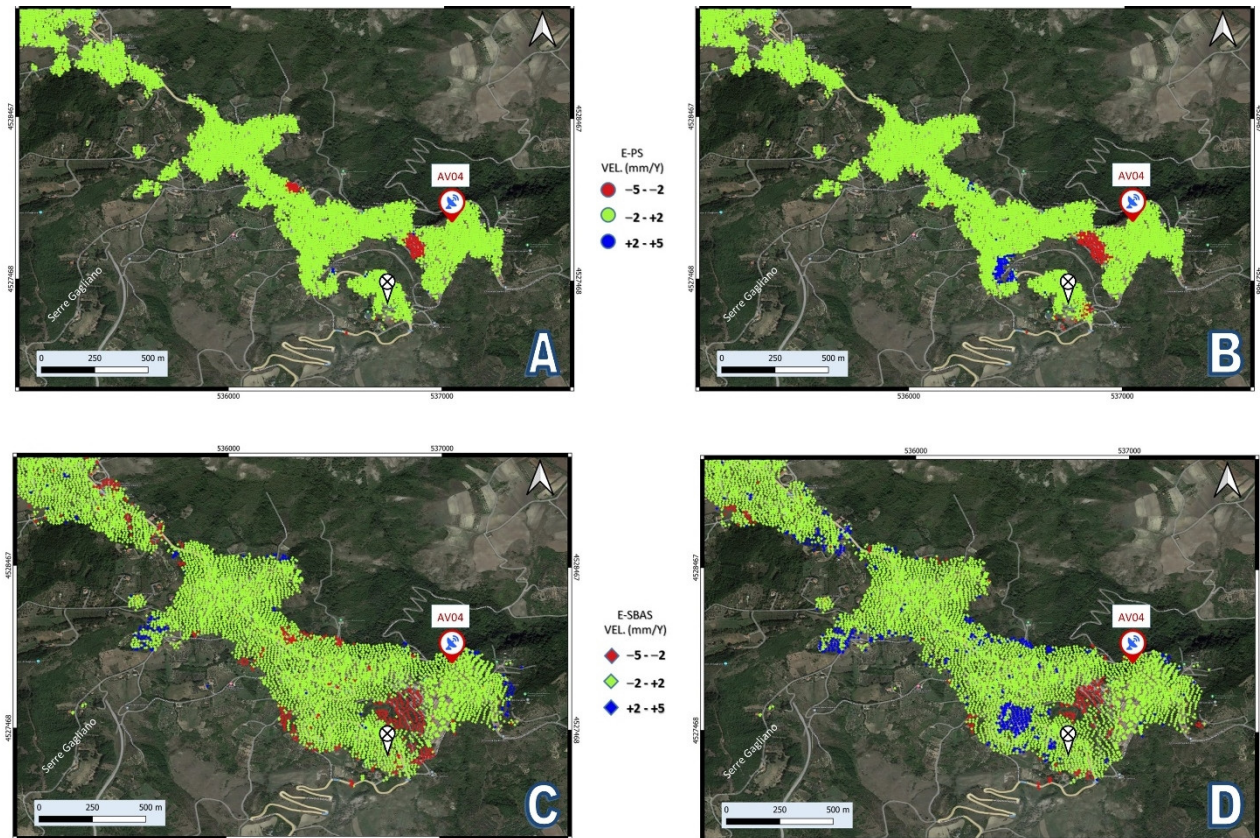


Figure 4. MTInSAR velocity (mm/Y) maps: (A) E-PS vertical; (B) E-PS east–west; (C) E-SBAS vertical; (D) E-SBAS east–west. For the vertical component maps, the negative values indicate a downward movement while positive values indicate an upward movement; for the E-W component maps, negative values indicate a westward movement while positive values indicate an eastward movement. The figures also show the locations of the GNSS stations of AV04, managed by INGV, and of the football stadium.

4.2. E-SBAS Velocity Maps

The velocity maps depicted in Figure 4C,D represent the distribution of monitorable points obtained with the E-SBAS algorithm for the vertical and E-W components, respectively. As the first result, a much larger area was covered, even obtaining information in the vegetated areas where the E-PS technique did not return any points. In the vertical component map, the main cluster of unstable points is located in the upper part of the southern slope, near Piazza della Repubblica. E-SBAS points, with negative velocity, are located both on buildings and in the most downstream vegetated area. Other clusters with the same velocity can be detected both on the southern and northern slopes of the Cortina basin. Unstable red points (i.e., negative velocity) are also located in the newest part of the town (toward NW), built up mainly after the 1980 earthquake.

Moreover, even the E-SBAS, which is also in the E-W component map, obtained points with a positive velocity (eastward). In that map, many clusters with positive velocity are visible all around the town and the largest one is located on the western slope. However, the main cluster characterized by negative velocity can be identified in correspondence with the upper part of the southern slope, as previously described in the other maps.

Other relevant dense clusters are shown in Serre Gagliano, in the NW portion of the study area, where there are different lithology outcrops (i.e., calcarenite).

4.3. IFFI Database Update

The E-PS and E-SBAS maps have overlapped with the landslide polygons contained in the IFFI database (Figure 5). Taking into account the outcomes of the E-PS analysis (E-W and vertical component maps), the identified clusters correspond to areas within mapped landslides or very close to them. In particular, Figure 5A (vertical component) and Figure 5B (E-W component) show E-PSs with negative velocity in the upper part of the slope and only in the horizontal component map, with positive velocity on the western flank of the main mass movement already known (dashed black line). Moreover, in the map of the vertical components and in the E-W map, the deformation area identified by the summit cluster (corresponding to the area near the old town) seems to be more extensive than that mapped. On the other hand, a significant portion of the landslide area shows stable behavior, as indicated by the E-PS points showing velocities between -2 and $+2$ mm/year.

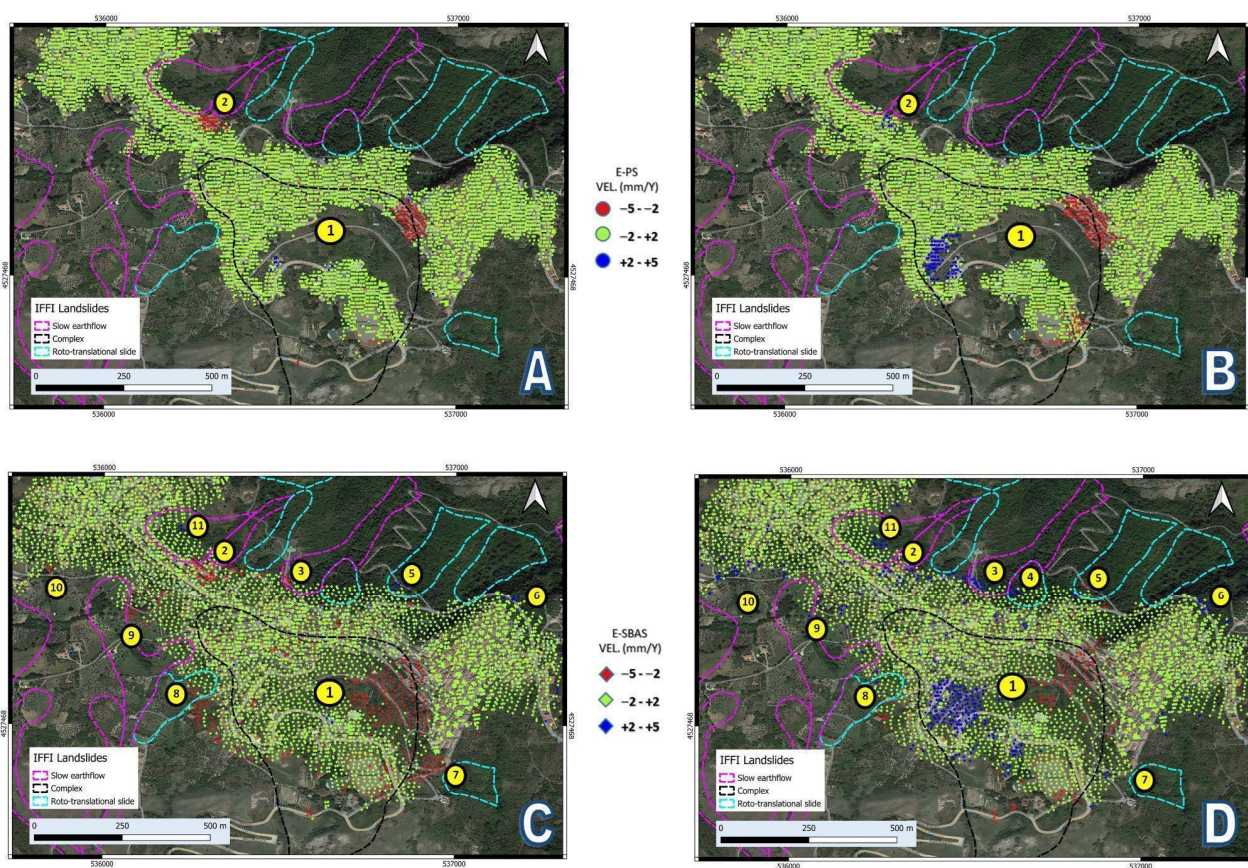


Figure 5. Comparison between landslides contained in the IFFI database (colored polygons) and velocity maps obtained with the algorithms E-PS ((A) vertical component, (B) E-W component) and E-SBAS ((C) vertical component, (D) E-W component). The numbers in the yellow dots correspond to the different clusters identified.

On the northern slope, the matching between the IFFI polygons and E-PS was almost impossible due to the lack of E-PSs. Only one cluster (Figure 4A), particularly evident in the vertical component map, matches with an already known landslide classified as dormant and slow earthflow in the IFFI database.

The E-SBAS component maps (Figure 5C,D) show a better match between the clusters identified and the landslides already mapped. In particular, the map of vertical components

contains clusters within or very close to several mass movements affecting the built-up areas and surrounding ones.

The deformation areas appear to be much larger than those mapped on both slopes analyzed. The same behavior can be seen in the E-W component map obtained where most of the clusters with red (westward) and blue (eastward) dots were geocoded into the deformation areas but other monitorable points are located outside the polygons, especially in the NW sector.

Moreover, to assess the state of activity of detected landslides, the time series of some representing PSs and DSs have been considered. Figure 6A presents the E-SBAS vertical component map and shows the evolution of displacements of two unstable points located in the main landslide area during the whole period of analysis.

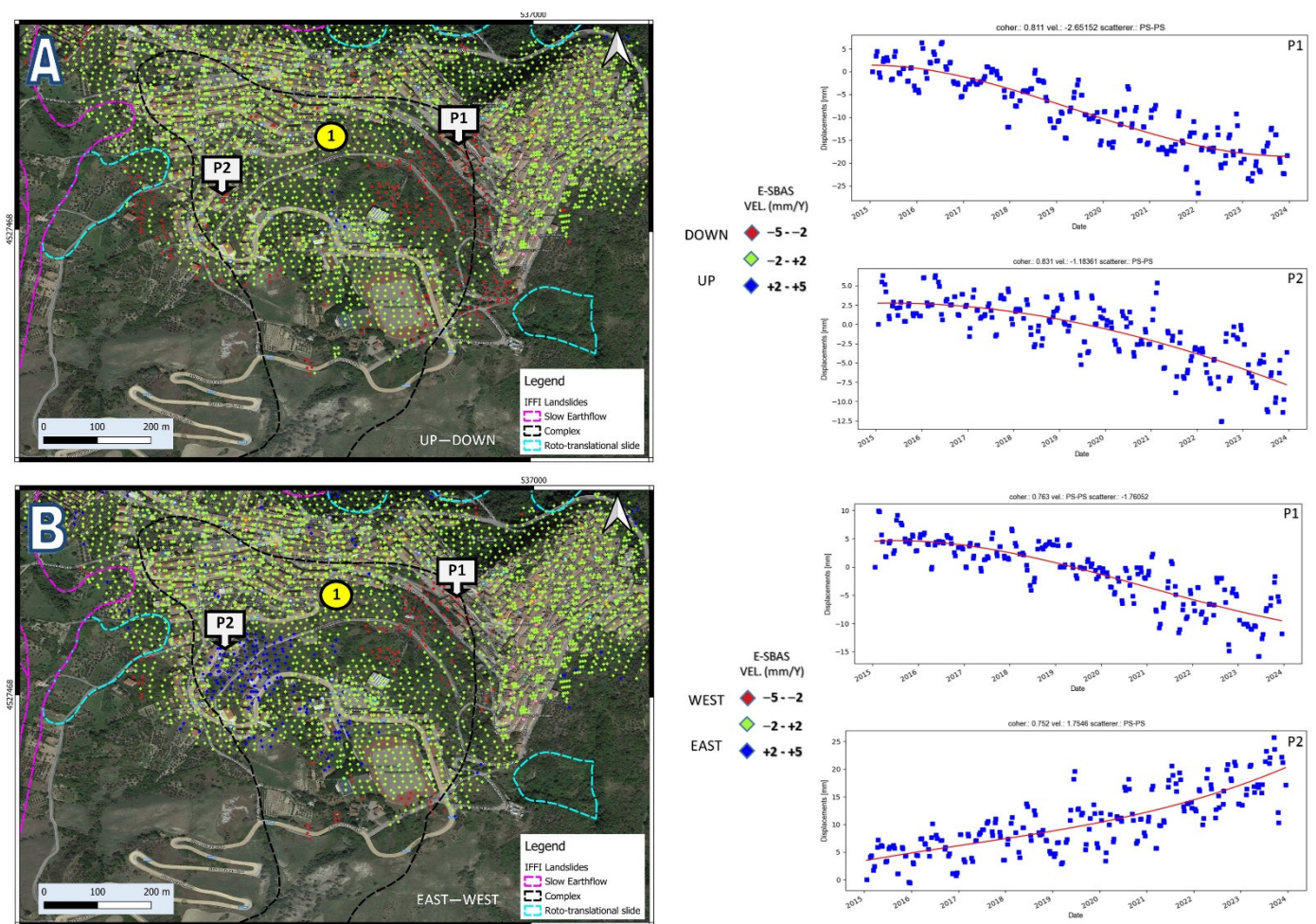


Figure 6. Focus on the “Calitri landslide” polygon (black dashed line) for the E-SBAS vertical (A) and E-W (B) component maps, respectively. The numbers in the yellow dots correspond to the different clusters identified.

P1 is located in the upper part of the town (near Piazza della Repubblica) and is characterized by a vertical cumulated displacement of about 2.5 cm; its velocity gradient seems to flatten from 2022.

P2 is on the western sector of the landslide area and its time series shows the first stable period (2015–2018) followed by an acceleration in the last 5 years with velocity > 2 mm/yr and a cumulated vertical displacement of about 1.2 cm.

The time series, shown in Figure 6B and referring to the E-W component map, seems to confirm the deformation trend and highlights a mass movement with complex kinematics. In fact, in this case, the P1 time series shows 3 cm of cumulated displacement while P2 has

positive velocity values that suggest a slide toward the east. These results are consistent with the hypothesis presented by several authors (mentioned in Sections 1 and 2) of a slow and deep mass movement, which involves pelitic terms (silty and marly clays, sands). Since historical times, the southern slope of the Calitri hill has been affected by a large complex landslide (which evolved into an earthflow).

Other PS and DS time series related to the northern slope have been considered and are shown in Figure 7A,B. According to the vertical component map, P3 and P4 present constant velocity rates, reaching cumulated displacements of 1.5 cm.

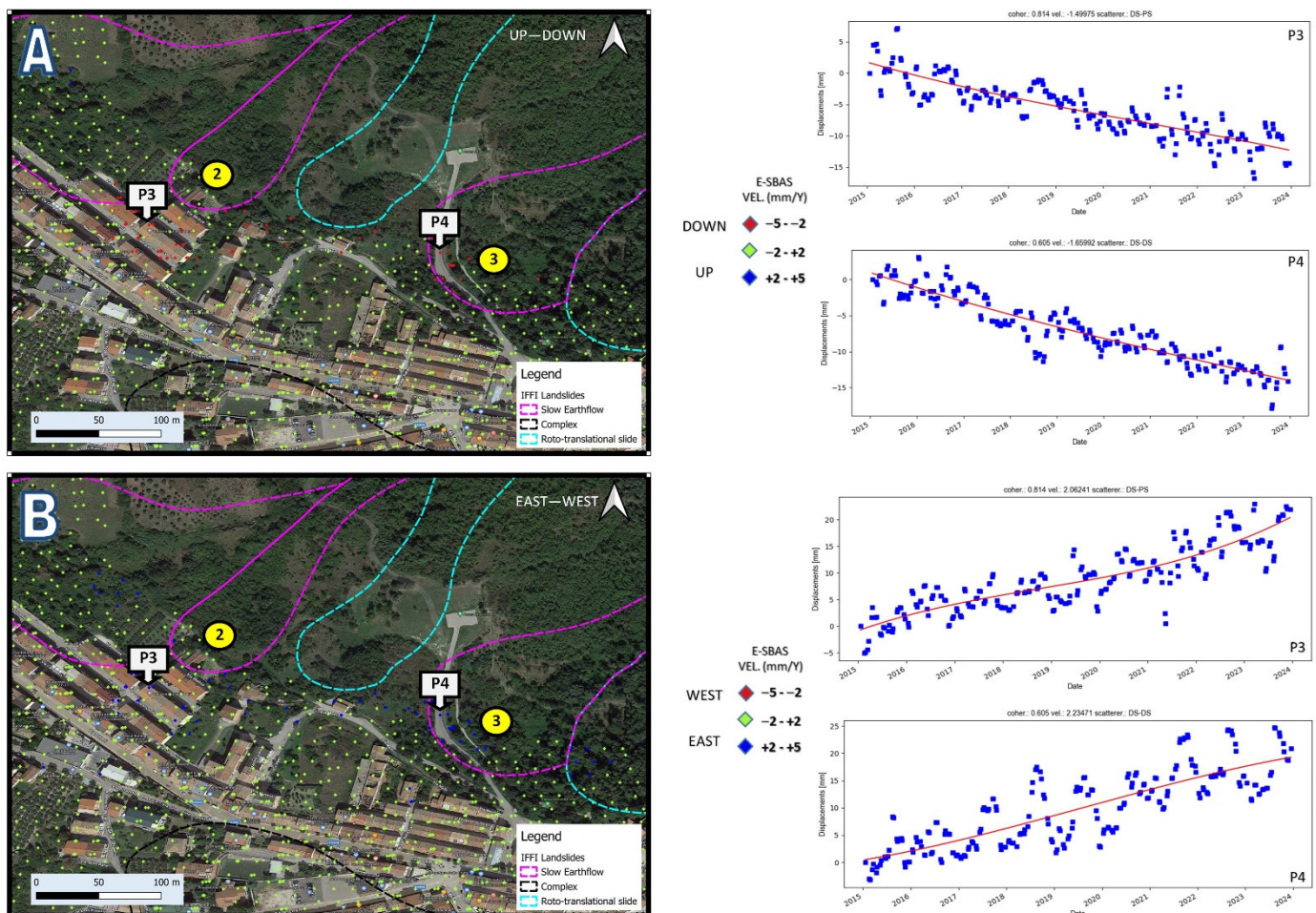


Figure 7. The northern slope of the Calitri town and a comparison between IFFI landslide polygons (colored dashed line) and the E-SBAS vertical (A) and E-W (B) component maps, respectively. The numbers in the yellow dots correspond to the different clusters identified.

Also, in the E-W component time series, the cumulated displacements of these points range between 2 and 2.5 cm, with positive values indicating a predominant east deformation component. Moreover, P3 and the cluster to which it belongs are located further upstream of the mapped area in the IFFI inventory. In this sector, clayey lithologies outcrop and the deformation phenomena identified correspond to slow, shallow landslides, considering the typical velocities of landslides involving fine-grained soils [62].

In the last cases, in Figure 8A,B, the temporal series of PSs and DSs placed near other minor landslides affecting the southern slope are shown.

P5 and its cluster have important cumulated deformation and are located in a vegetated area very close to the main mass movement body. However, a topographic ridge separates the two phenomena with different kinematics.

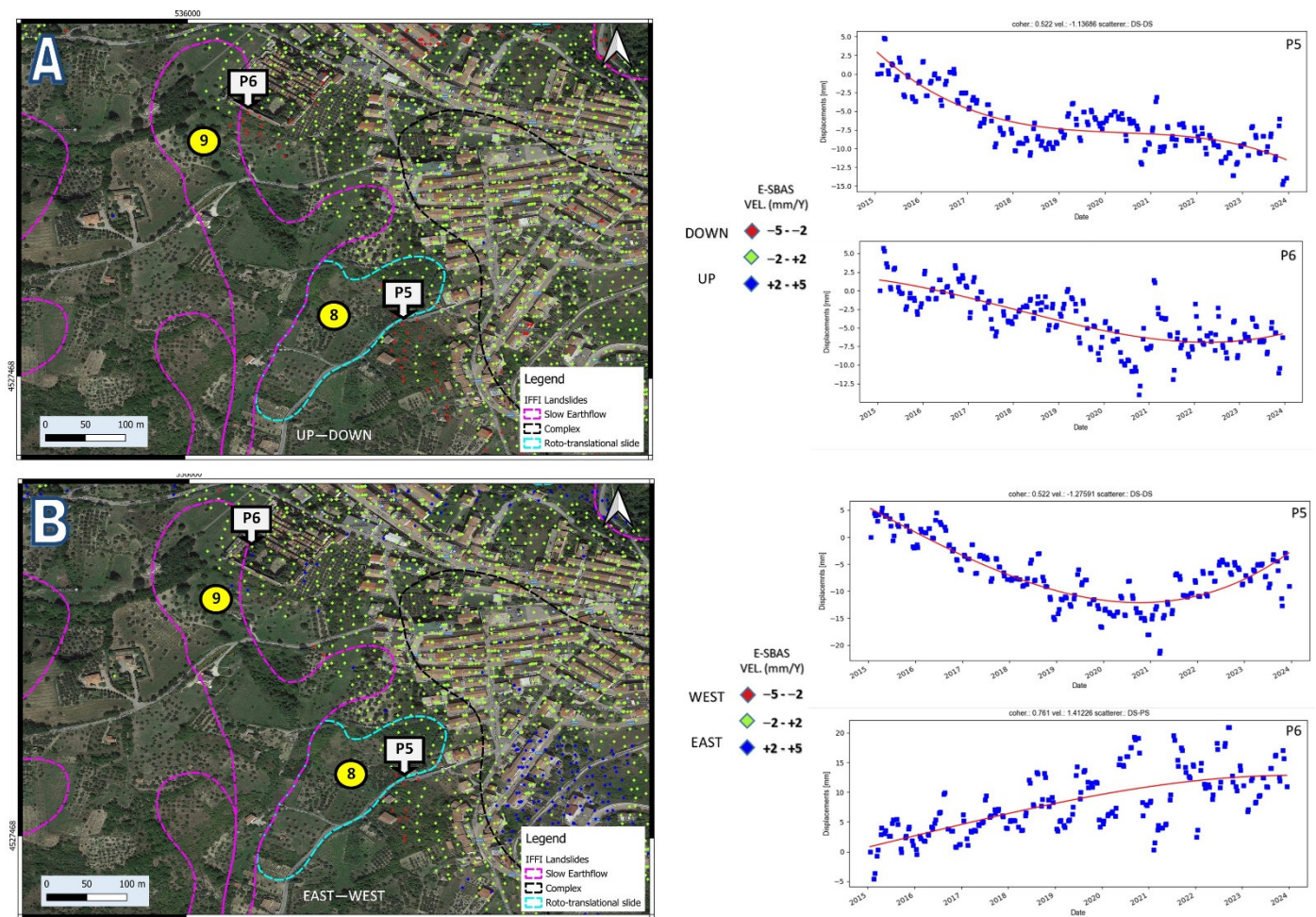


Figure 8. The NW sector of the Calitri town and a comparison between IFFI landslide polygons (colored dashed line) and the E-SBAS vertical (A) and E-W (B) component maps, respectively. The numbers in the yellow dots correspond to the different clusters identified.

P6 belongs to a cluster located in the cemetery of the town and the ongoing deformations are very dangerous, also considering the social importance of the site. In fact, the cemetery area shows a continuous deformation like other residential areas but can be considered a place to be carefully monitored for its structural and sociological delicacy.

The time series exhibit noticeable periodic fluctuations, likely attributed to seasonal effects. This behavior, particularly pronounced for certain points (e.g., P1, P2, and P4), appears to occur annually and is consistent across all detected clusters.

5. Discussion

The conducted study on the Calitri municipality has shown how the new MTInSAR algorithm employed is particularly well suited to detect and monitor landslides in urban and suburban areas and to assess their state of activity.

For this purpose, the study area represents a great test site, considering that only relatively slow landslides (<100 mm/yr; [5]) can be detected and monitored effectively by MTInSAR analysis, and previous works have already assessed the velocity of landslides affecting that area from slow to very slow [14,15]. E-PS is very affordable in urbanized areas, returning 14,581 monitorable points. On the other hand, E-SBAS successfully investigates the peri-urban areas, producing 11,800 monitorable points, which encompass both persistent scatterers (PSs) and distributed scatterers (DSs), even in vegetated areas.

Taking into account information from the E-W and vertical component maps achieved through both E-PS and E-SBAS techniques, the landslides affecting the built-up and sub-

urban areas of Calitri consist of roto-translational slides and associated earth flows. The analysis of time series suggests that these phenomena have consistently moved in the last decade, increasingly enlarging their extent, both on the northern and southern slopes. Moreover, the E-W component maps show different directions in the evolution of the earth flow and roto-translational flow, some toward the east and others toward the west, according to the topography (Figure 9). The detected landslides develop in a complex geological environment, characterized by lithologies with different rheological behaviors (i.e., brittle/ductile lithotypes referred to as clay, silty clay, and sandstone outcroppings).



Figure 9. Map representing displacement vectors for each cluster detected in the study area. The arrow's dimension is proportional to the cluster dimension (both E-W and vertical). The arrow's curve gives qualitative information on the kinematics of the corresponding mass movement.

This study highlights how, within the main mass movement affecting the southern slope reactivated after the 1980 earthquake, sectors with different kinematics can be identified. In particular, the main deformations detected in that area regard the upper part of the slope, corresponding with Piazza della Repubblica, where it is assumed that the slip surface is near the ground level. The cluster located there is characterized by a considerable vertical deformation in association with a western component.

The other main cluster is located on the western flank of the main landslide and has a predominant eastern component (Figure 9). Additionally, outcomes suggest that the NW and the intermediate sectors of the black dashed line polygon can be considered stable while other relevant movements have been detected in the area immediately below the football stadium.

Furthermore, other unstable areas depicted with orange arrows in Figure 9 are present all around the town and some of them do not correspond to already known and mapped landslides, especially for the northern slope of the Cortino basin, according to the IFFI database (updated to 2006).

The results provide a good instrument for quick and precise analysis and should be confirmed through a comparison with in situ measurements. However, although many

geognostic investigations were carried out in the area after the earthquake, and dozens of boreholes were equipped with inclinometers or piezometers, it was not possible to obtain data coeval with the period covered by satellite imagery. Most of the instrumentation has been abandoned or unusable for many years. To compensate for this lack, photographic surveys were carried out to look for field evidence in areas immediately near the clusters identified, yielding a good response, as shown in Figure 10.

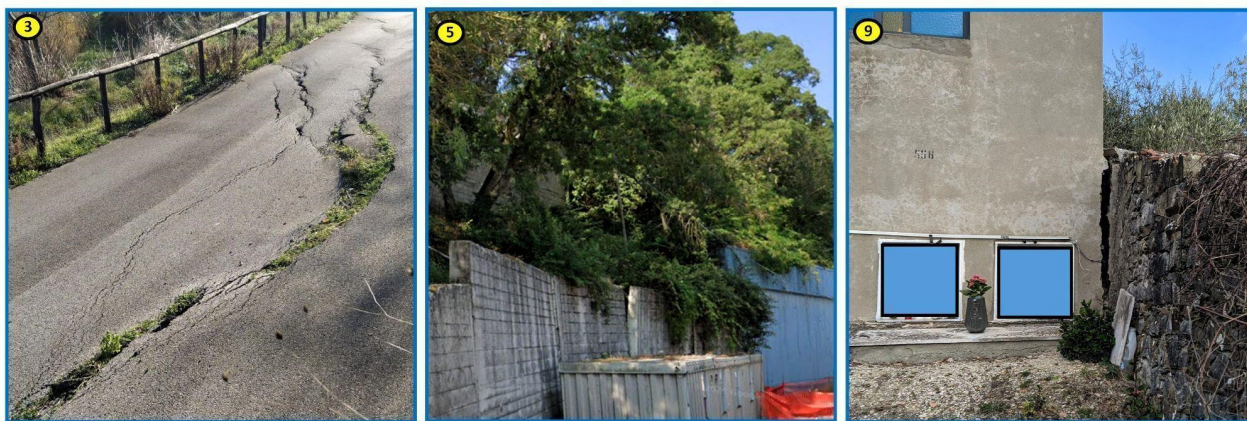


Figure 10. Photographic surveys (2 February 2024) were conducted to search for field evidence in areas immediately near some of the identified clusters. The numbers in the yellow circles identify the clusters of points where the photos were taken.

So, the approaches and new algorithms used to investigate the Calitri territory are available for large areas worldwide, allowing the potential investigation of active landslides in different geographic and climatic contexts, particularly in those landslide areas where long-term ground-based measurements are not available. Areas prone to landslides generally encompass slopes where many predisposing factors coexist (lithology, land use, soil texture, elevation, slope gradient, slope aspect, local relief, plan curvature, profile curvature, etc.). Therefore, both techniques offer enhanced monitoring capabilities for landslides, improving coverage and resolution. The E-PS algorithm, in particular, provides superior coverage by effectively detecting DSs in areas with arboreal vegetation, where traditional PS methods might fail. Conversely, the E-SBAS algorithm enhances resolution through the use of oversampled interferograms, enabling a more nuanced analysis of areas containing even PS-like targets.

In various Euro-Mediterranean urban areas, slow-moving landslides pose a significant threat, potentially causing structural and infrastructural damage over time. While these landslides rarely result in loss of life, their gradual spatiotemporal evolution increases the structural vulnerability of the built environment, amplifying the risk. Addressing this challenge requires effective and sustainable risk mitigation strategies involving stakeholders. To this purpose, Landslide Inventory Maps (LIMs) should be (and in many cases are) widely used by authorities for land use management and planning activities, representing a valuable tool used to assist decision-makers in urban and infrastructural planning.

MTInSAR techniques contribute to improving the accuracy of an LIM and the prediction reliability of slow-moving landslides, which particularly affect urbanized areas. The results that can be achieved by monitoring the territory through this type of approach depend on the techniques used and the characteristics of the acquired imagery. L-band SAR images can be very useful in monitoring vegetated areas with few targets (both natural and artificial); X-band images, on the other hand, are widely used for the monitoring of deformations affecting buildings and infrastructure, thanks to their high spatial resolution. In this study, the C-band products, processed using the E-PS and E-SBAS algorithms, provided good coverage of the study area and allowed for monitoring points in both urbanized and vegetated areas. The integrated utilization of MTInSAR techniques maximizes the

benefits derived from satellite datasets. This includes leveraging the long-term series of displacements to comprehend the temporal evolution of the slope. Additionally, spatially dense deformation maps prove invaluable for precise activity mapping, as well as for the accurate assessment of vulnerability and damage in areas affected by active landslides.

6. Conclusions

In this study, two advanced MTInSAR algorithms were employed to comprehensively investigate mass movements affecting the hills and residential neighborhoods in the municipality of Calitri, southern Italy.

The application of E-PS and E-SBAS techniques to Sentinel-1 C-band images facilitated the production of deformation velocity maps for the study area retrieving E-W and vertical component maps. The high density of measurable points enabled the identification and precise location of clusters within previously mapped landslide polygons (IFFI database), as well as in the surrounding areas. Moreover, this approach also allowed us to evaluate the contribution of the E-W and vertical components in the deformation processes. Examining the time series of E-PS and E-SBAS and their displacement rates, the state of activity of the detected landslides was investigated. The main phenomenon, known as the “Calitri landslide”, consists of a deep-seated rotational/translational slide and other associated earthflows, so it could be considered a landslide complex. This landslide, which has been active for at least the last four decades, has caused significant damage to the historic center of the town and appears to be the latest in a series of events impacting the southern slope and influencing its topography. The time series analysis indicates constant slow movements of the upper and western sectors of the slide while other sub-regions are characterized by the presence of stable points.

Several previous works focused on the main landslide affecting the southern slope, which was reactivated after the 1980 Irpinia earthquake, but many active mass movements also affect the northern slope, as confirmed by the present analysis.

This result confirms the possibility of mapping landslide activity in urban and suburban areas and the very good reliability of employed algorithms, aligning with results from previous DInSAR analyses in the same territory. Moreover, as confirmed in a lot of already published contributions, these techniques can be used for landslide inventory updating. To proceed effectively, the outcomes should be integrated with field surveys and conventional thematic data for accurate application and interpretation, where possible. In this study, the outputs enabled the observation of several zones affected by active landslides, validating, and updating the landslide inventory. Numerous landslides previously classified as active, reactivated, or dormant were confirmed to be undergoing deformation, while in other cases, new deformation phenomena not already mapped in the IFFI database were detected.

Author Contributions: Conceptualization, N.A.F.; methodology, N.A.F. and P.M.; software, N.A.F., M.D., A.C., P.R. and G.T.; data processing, N.A.F. and P.R.; validation, All; investigation, All; data curation, N.A.F. and P.M.; writing—original draft preparation, All; writing—review and editing, All; supervision, N.A.F. and P.M. All authors have read and agreed to the published version of the manuscript.

Funding: This research received no external funding.

Data Availability Statement: Sentinel data were made available by ESA in the Copernicus project through the Open Access Hub portal (<https://scihub.copernicus.eu/dhus/#/home> (accessed on 10 January 2024)).

Acknowledgments: Sentinel data, from the ESA Copernicus Project, were obtained through the Open Access Hub (<https://scihub.copernicus.eu/dhus/#/home>, accessed on 10 January 2024). MTInSAR processing and data modeling were carried out with ENVI[®] SARscape[®] (Sarmap, CH).

Conflicts of Interest: Authors Marco Defilippi, Alessio Cantone, Paolo Riccardi and Giulia Tessari were employed by the company SarmapSA. The remaining authors declare that the research was conducted in the absence of any commercial or financial relationships that could be construed as a potential conflict of interest.

References

1. Donati, L.; Turrini, M.C. An Objective Method to Rank the Importance of the Factors Predisposing to Landslides with the GIS Methodology: Application to an Area of the Apennines (Valnerina; Perugia, Italy). *Eng. Geol.* **2002**, *63*, 277–289. [\[CrossRef\]](#)
2. Wang, L.-J.; Guo, M.; Sawada, K.; Lin, J.; Zhang, J. Landslide Susceptibility Mapping in Mizunami City, Japan: A Comparison between Logistic Regression, Bivariate Statistical Analysis and Multivariate Adaptive Regression Spline Models. *CATENA* **2015**, *135*, 271–282. [\[CrossRef\]](#)
3. Conforti, M.; Ietto, F. Modeling Shallow Landslide Susceptibility and Assessment of the Relative Importance of Predisposing Factors, through a GIS-Based Statistical Analysis. *Geosciences* **2021**, *11*, 333. [\[CrossRef\]](#)
4. Varnes, D. *Slope Movement Types and Processes*; Transportation Research Board: Washington, DC, USA, 1978.
5. Cruden, D.; Varnes, D. *Landslide Types and Processes*; Transportation Research Board: Washington, DC, USA; US National Academy of Sciences: Washington, DC, USA, 1996; pp. 36–57.
6. Hungr, O.; Leroueil, S.; Picarelli, L. The Varnes Classification of Landslide Types, an Update. *Landslides* **2014**, *11*, 167–194. [\[CrossRef\]](#)
7. Petley, D. Global Patterns of Loss of Life from Landslides. *Geology* **2012**, *40*, 927–930. [\[CrossRef\]](#)
8. Vranken, L.; Van Turnhout, P.; Van Den Eeckhaut, M.; Vandekerckhove, L.; Poesen, J. Economic Valuation of Landslide Damage in Hilly Regions: A Case Study from Flanders, Belgium. *Sci. Total Environ.* **2013**, *447*, 323–336. [\[CrossRef\]](#) [\[PubMed\]](#)
9. Liu, W.; Yan, S.; He, S. Landslide Damage Incurred to Buildings: A Case Study of Shenzhen Landslide. *Eng. Geol.* **2018**, *247*, 69–83. [\[CrossRef\]](#)
10. Guerriero, L.; Confuorto, P.; Calcaterra, D.; Guadagno, F.M.; Revellino, P.; Di Martire, D. PS-Driven Inventory of Town-Damaging Landslides in the Benevento, Avellino and Salerno Provinces, Southern Italy. *J. Maps* **2019**, *15*, 619–625. [\[CrossRef\]](#)
11. Matano, F. Analysis and Classification of Natural and Human-Induced Ground Deformations at Regional Scale (Campania, Italy) Detected by Satellite Synthetic-Aperture Radar Interferometry Archive Datasets. *Remote Sens.* **2019**, *11*, 2822. [\[CrossRef\]](#)
12. Vicari, A.; Famiglietti, N.A.; Colangelo, G.; Cecere, G. A Comparison of Multi Temporal Interferometry Techniques for Landslide Susceptibility Assessment in Urban Area: An Example on Stigliano (MT), a Town of Southern of Italy. *Geomat. Nat. Hazards Risk* **2019**, *10*, 836–852. [\[CrossRef\]](#)
13. Guzzetti, F.; Mondini, A.C.; Cardinali, M.; Fiorucci, F.; Santangelo, M.; Chang, K.-T. Landslide Inventory Maps: New Tools for an Old Problem. *Earth-Sci. Rev.* **2012**, *112*, 42–66. [\[CrossRef\]](#)
14. Calò, F.; Calcaterra, D.; Iodice, A.; Parise, M.; Ramondini, M. Assessing the Activity of a Large Landslide in Southern Italy by Ground-Monitoring and SAR Interferometric Techniques. *Int. J. Remote Sens.* **2012**, *33*, 3512–3530. [\[CrossRef\]](#)
15. Martire, D.D.; De Luca, G.; Ramondini, M.; Calcaterra, D. Landslide-Related PS Data Interpretation by Means of Different Techniques. In *Landslide Science and Practice: Volume 2: Early Warning, Instrumentation and Monitoring*; Margottini, C., Canuti, P., Sassa, K., Eds.; Springer: Berlin/Heidelberg, Germany, 2013; pp. 347–355. ISBN 978-3-642-31445-2.
16. Borgia, A.; Tizzani, P.; Solaro, G.; Manzo, M.; Casu, F.; Luongo, G.; Pepe, A.; Bernardino, P.; Fornaro, G.; Sansosti, E.; et al. Volcanic Spreading of Vesuvius, a New Paradigm for Interpreting Its Volcanic Activity. *Geophys. Res. Lett.* **2005**, *32*, 3. [\[CrossRef\]](#)
17. Bell, J.W.; Amelung, F.; Henry, C.D. InSAR Analysis of the 2008 Reno-Mogul Earthquake Swarm: Evidence for Westward Migration of Walker Lane Style Dextral Faulting. *Geophys. Res. Lett.* **2012**, *39*. [\[CrossRef\]](#)
18. Cascini, L.; Calvello, M.; Grimaldi, G.M. Groundwater Modeling for the Analysis of Active Slow-Moving Landslides. *J. Geotech. Geoenvironmental Eng.* **2010**, *136*, 1220–1230. [\[CrossRef\]](#)
19. Avallone, A.; Cirella, A.; Cheloni, D.; Tolomei, C.; Theodoulidis, N.; Piatanesi, A.; Briole, P.; Ganas, A. Near-Source High-Rate GPS, Strong Motion and InSAR Observations to Image the 2015 Lefkada (Greece) Earthquake Rupture History. *Sci. Rep.* **2017**, *7*, 10358. [\[CrossRef\]](#) [\[PubMed\]](#)
20. Confuorto, P.; Casagli, N.; Casu, F.; De Luca, C.; Del Soldato, M.; Festa, D.; Lanari, R.; Manzo, M.; Onorato, G.; Raspini, F. Sentinel-1 P-SBAS Data for the Update of the State of Activity of National Landslide Inventory Maps. *Landslides* **2023**, *20*, 1083–1097. [\[CrossRef\]](#)
21. Plank, S.; Twele, A.; Martinis, S. Landslide Mapping in Vegetated Areas Using Change Detection Based on Optical and Polarimetric SAR Data. *Remote Sens.* **2016**, *8*, 307. [\[CrossRef\]](#)
22. Park, S.-E.; Lee, S.-G. On the Use of Single-, Dual-, and Quad-Polarimetric SAR Observation for Landslide Detection. *ISPRS Int. J. Geo-Inf.* **2019**, *8*, 384. [\[CrossRef\]](#)
23. Ge, P.; Gokon, H.; Meguro, K.; Koshimura, S. Study on the Intensity and Coherence Information of High-Resolution ALOS-2 SAR Images for Rapid Massive Landslide Mapping at a Pixel Level. *Remote Sens.* **2019**, *11*, 2808. [\[CrossRef\]](#)
24. Burrows, K.; Walters, R.J.; Milledge, D.; Densmore, A.L. A Systematic Exploration of Satellite Radar Coherence Methods for Rapid Landslide Detection. *Nat. Hazards Earth Syst. Sci.* **2020**, *20*, 3197–3214. [\[CrossRef\]](#)
25. Raspini, F.; Ciampalini, A.; Del Conte, S.; Lombardi, L.; Nocentini, M.; Gigli, G.; Ferretti, A.; Casagli, N. Exploitation of Amplitude and Phase of Satellite SAR Images for Landslide Mapping: The Case of Montescaglioso (South Italy). *Remote Sens.* **2015**, *7*, 14576–14596. [\[CrossRef\]](#)
26. Tessari, G.; Floris, M.; Pasquali, P. Phase and Amplitude Analyses of SAR Data for Landslide Detection and Monitoring in Non-Urban Areas Located in the North-Eastern Italian Pre-Alps. *Environ. Earth Sci.* **2017**, *76*, 85. [\[CrossRef\]](#)
27. Mondini, A.C.; Santangelo, M.; Rocchetti, M.; Rossetto, E.; Manconi, A.; Monserrat, O. Sentinel-1 SAR Amplitude Imagery for Rapid Landslide Detection. *Remote Sens.* **2019**, *11*, 760. [\[CrossRef\]](#)

28. Miele, P.; Di Napoli, M.; Novellino, A.; Calcaterra, D.; Mallorqui, J.J.; Di Martire, D. SAR Data and Field Surveys Combination to Update Rainfall-Induced Shallow Landslide Inventory. *Remote Sens. Appl. Soc. Environ.* **2022**, *26*, 100755. [[CrossRef](#)]
29. Perissin, D. Interferometric SAR Multitemporal Processing: Techniques and Applications. In *Multitemporal Remote Sensing: Methods and Applications*; Ban, Y., Ed.; Springer International Publishing: Cham, Switzerland, 2016; pp. 145–176. ISBN 978-3-319-47037-5.
30. Devara, M.; Tiwari, A.; Dwivedi, R. Landslide Susceptibility Mapping Using MT-InSAR and AHP Enabled GIS-Based Multi-Criteria Decision Analysis. *Geomat. Nat. Hazards Risk* **2021**, *12*, 675–693. [[CrossRef](#)]
31. Casagli, N.; Intrieri, E.; Tofani, V.; Gigli, G.; Raspini, F. Landslide Detection, Monitoring and Prediction with Remote-Sensing Techniques. *Nat. Rev. Earth Environ.* **2023**, *4*, 51–64. [[CrossRef](#)]
32. Lu, C.-Y.; Chan, Y.-C.; Hu, J.-C.; Chiu, C.-Y.; Chu, C.-R.; Tseng, C.-H.; Chang, C.-H. Velocity Distribution and Movement of Multiple Slow-Moving Landslides Characterized by an Optimized MTInSAR Workflow. *Eng. Geol.* **2023**, *327*, 107339. [[CrossRef](#)]
33. Solari, L.; Del Soldato, M.; Raspini, F.; Barra, A.; Bianchini, S.; Confuorto, P.; Casagli, N.; Crosetto, M. Review of Satellite Interferometry for Landslide Detection in Italy. *Remote Sens.* **2020**, *12*, 1351. [[CrossRef](#)]
34. Navarro, J.A.; Tomás, R.; Barra, A.; Pagán, J.I.; Reyes-Carmona, C.; Solari, L.; Vinielles, J.L.; Falco, S.; Crosetto, M. ADAtools: Automatic Detection and Classification of Active Deformation Areas from PSI Displacement Maps. *ISPRS Int. J. Geo-Inf.* **2020**, *9*, 584. [[CrossRef](#)]
35. Guzzetti, F.; Ardizzone, F.; Cardinali, M.; Rossi, M.; Valigi, D. Landslide Volumes and Landslide Mobilization Rates in Umbria, Central Italy. *Earth Planet. Sci. Lett.* **2009**, *279*, 222–229. [[CrossRef](#)]
36. Bovenga, F.; Wasowski, J.; Nitti, D.O.; Nutricato, R.; Chiaradia, M.T. Using COSMO/SkyMed X-Band and ENVISAT C-Band SAR Interferometry for Landslides Analysis. *Remote Sens. Environ.* **2012**, *119*, 272–285. [[CrossRef](#)]
37. Del Soldato, M.; Riquelme, A.; Bianchini, S.; Tomàs, R.; Di Martire, D.; De Vita, P.; Moretti, S.; Calcaterra, D. Multisource Data Integration to Investigate One Century of Evolution for the Agnone Landslide (Molise, Southern Italy). *Landslides* **2018**, *15*, 2113–2128. [[CrossRef](#)]
38. Moretto, S.; Bozzano, F.; Mazzanti, P. The Role of Satellite InSAR for Landslide Forecasting: Limitations and Openings. *Remote Sens.* **2021**, *13*, 3735. [[CrossRef](#)]
39. Chen, X.; Tessari, G.; Fabris, M.; Achilli, V.; Floris, M. Comparison Between PS and SBAS InSAR Techniques in Monitoring Shallow Landslides. In *Understanding and Reducing Landslide Disaster Risk: Volume 3 Monitoring and Early Warning*; Casagli, N., Tofani, V., Sassa, K., Bobrowsky, P.T., Takara, K., Eds.; Springer International Publishing: Cham, Switzerland, 2021; pp. 155–161; ISBN 978-3-030-60311-3.
40. Liu, X.; Zhao, C.; Zhang, Q.; Peng, J.; Zhu, W.; Lu, Z. Multi-Temporal Loess Landslide Inventory Mapping with C-, X- and L-Band SAR Datasets—A Case Study of Heifangtai Loess Landslides, China. *Remote Sens.* **2018**, *10*, 1756. [[CrossRef](#)]
41. Zhao, C.; Kang, Y.; Zhang, Q.; Lu, Z.; Li, B. Landslide Identification and Monitoring along the Jinsha River Catchment (Wudongde Reservoir Area), China, Using the InSAR Method. *Remote Sens.* **2018**, *10*, 993. [[CrossRef](#)]
42. Wasowski, J.; Bovenga, F. Chapter 11—Remote Sensing of Landslide Motion with Emphasis on Satellite Multi-Temporal Interferometry Applications: An Overview. In *Landslide Hazards, Risks, and Disasters*, 2nd ed.; Davies, T., Rosser, N., Shroder, J.F., Eds.; Hazards and Disasters Series; Elsevier: Amsterdam, The Netherlands, 2022; pp. 365–438. ISBN 978-0-12-818464-6.
43. Ferretti, A.; Savio, G.; Barzaghi, R.; Borghi, A.; Musazzi, S.; Novali, F.; Prati, C.; Rocca, F. Submillimeter Accuracy of InSAR Time Series: Experimental Validation. *IEEE Trans. Geosci. Remote Sens.* **2007**, *45*, 1142–1153. [[CrossRef](#)]
44. Osmanoglu, B.; Sunar, F.; Wdowinski, S.; Cabral-Cano, E. Time Series Analysis of InSAR Data: Methods and Trends. *ISPRS J. Photogramm. Remote Sens.* **2016**, *115*, 90–102. [[CrossRef](#)]
45. Cigna, F.; Esquivel Ramírez, R.; Tapete, D. Accuracy of Sentinel-1 PSI and SBAS InSAR Displacement Velocities against GNSS and Geodetic Leveling Monitoring Data. *Remote Sens.* **2021**, *13*, 4800. [[CrossRef](#)]
46. Monti, L.; D’Elia, G.; Toccaceli, R.M. 20. Analisi del Dissesto da Frana in Campania. Available online: https://www.isprambiente.gov.it/files/pubblicazioni/rapporti/rapporto-frane-2007/Capitolo_20_Campania.pdf (accessed on 10 January 2024).
47. D’Argenio, B.; Pescatore, T.; Scandone, P. Schema Geologico Dell’Appennino Meridionale (Campania e Lucania). *Atti Convegno Bmoderne Vedute Geol. Dell’appenninoq* **1973**, *183*, 220–248.
48. Martino, S.; Scarascia Mugnozza, G. The Role of the Seismic Trigger in the Calitri Landslide (Italy): Historical Reconstruction and Dynamic Analysis. *Soil Dyn. Earthq. Eng.* **2005**, *25*, 933–950. [[CrossRef](#)]
49. Hutchinson, J.N.; Del Prete, M. Landslides at Calitri, Southern Apennines, Reactivated by the Earthquake of 23rd November 1980. *Geol. Appl. Idrogeol.* **1985**, *20*, 9.
50. Santo, A.; Budetta, P.; Calcaterra, D.; Ducci, D.; Corniello, A.; de Riso, R.; Corniello, A. Appunti Di Geologia Dell’Appennino Meridionale Con Riferimento Ai “Rischi” Ed Alle Risorse Del Territorio. In *Memorie e Note Dell’istituto di Geologia Applicata Dell’universita di Napoli*; STAMPA: Bregaglia, Switzerland, 1993; pp. 1–63.
51. Parise, M.; Wasowski, J. Landslide Activity Maps for Landslide Hazard Evaluation: Three Case Studies from Southern Italy. *Nat. Hazards* **1999**, *20*, 159–183. [[CrossRef](#)]
52. Crosetto, M.; Monserrat, O.; Cuevas-González, M.; Devanthery, N.; Crippa, B. Persistent Scatterer Interferometry: A Review. *ISPRS J. Photogramm. Remote Sens.* **2016**, *115*, 78–89. [[CrossRef](#)]
53. Li, S.; Xu, W.; Li, Z. Review of the SBAS InSAR Time-Series Algorithms, Applications, and Challenges. *Geod. Geodyn.* **2022**, *13*, 114–126. [[CrossRef](#)]

54. Ferretti, A.; Prati, C.; Rocca, F. Permanent Scatterers in SAR Interferometry. *IEEE Trans. Geosci. Remote Sens.* **2001**, *39*, 8–20. [[CrossRef](#)]
55. Berardino, P.; Fornaro, G.; Lanari, R.; Sansosti, E. A New Algorithm for Surface Deformation Monitoring Based on Small Baseline Differential SAR Interferograms. *IEEE Trans. Geosci. Remote Sens.* **2002**, *40*, 2375–2383. [[CrossRef](#)]
56. Jung, J.; Kim, D.; Park, S.-E. Correction of Atmospheric Phase Screen in Time Series InSAR Using WRF Model for Monitoring Volcanic Activities. *IEEE Trans. Geosci. Remote Sens.* **2014**, *52*, 2678–2689. [[CrossRef](#)]
57. Ferretti, A.; Fumagalli, A.; Novali, F.; Prati, C.; Rocca, F.; Rucci, A. A New Algorithm for Processing Interferometric Data-Stacks: SqueeSAR. *IEEE Trans. Geosci. Remote Sens.* **2011**, *49*, 3460–3470. [[CrossRef](#)]
58. Fornaro, G.; Verde, S.; Reale, D.; Pauciuolo, A. CAESAR: An Approach Based on Covariance Matrix Decomposition to Improve Multibaseline–Multitemporal Interferometric SAR Processing. *IEEE Trans. Geosci. Remote Sens.* **2015**, *53*, 2050–2065. [[CrossRef](#)]
59. Ferretti, A.; Prati, C.; Rocca, F. Nonlinear Subsidence Rate Estimation Using Permanent Scatterers in Differential SAR Interferometry. *IEEE Trans. Geosci. Remote Sens.* **2000**, *38*, 2202–2212. [[CrossRef](#)]
60. Fialko, Y.; Simons, M.; Agnew, D. The Complete (3-D) Surface Displacement Field in the Epicentral Area of the 1999 MW7.1 Hector Mine Earthquake, California, from Space Geodetic Observations. *Geophys. Res. Lett.* **2001**, *28*, 3063–3066. [[CrossRef](#)]
61. Ng, A.H.-M.; Ge, L.; Zhang, K.; Chang, H.-C.; Li, X.; Rizos, C.; Omura, M. Deformation Mapping in Three Dimensions for Underground Mining Using InSAR—Southern Highland Coalfield in New South Wales, Australia. *Int. J. Remote Sens.* **2011**, *32*, 7227–7256. [[CrossRef](#)]
62. Hungr, O.; Eberhardt, J.C.E. Estimating Landslide Motion Mechanism, Travel Distance and Velocity. In *Landslide Risk Management*; CRC Press: Boca Raton, FL, USA, 2005; ISBN 978-0-429-15135-4.

Disclaimer/Publisher’s Note: The statements, opinions and data contained in all publications are solely those of the individual author(s) and contributor(s) and not of MDPI and/or the editor(s). MDPI and/or the editor(s) disclaim responsibility for any injury to people or property resulting from any ideas, methods, instructions or products referred to in the content.